

Two types of summertime heating over the Asian large-scale orography and excitation of potential-vorticity forcing I. Over Tibetan Plateau

WU GuoXiong¹, ZHUO HaiFeng^{1,2}, WANG ZiQian^{3,1*} & LIU YiMin^{1†}

¹State Key Laboratory of Numerical Modeling for Atmospheric Sciences and Geophysical Fluid Dynamics, Institute of Atmospheric Physics, Chinese Academy of Sciences, Beijing 100029, China;

²College of Earth Sciences, University of Chinese Academy of Sciences, Beijing 100049, China;

³School of Atmospheric Sciences, Sun Yat-sen University, Guangzhou 510275, China

Received January 4, 2016; accepted April 12, 2016; published online August 8, 2016

Abstract Based on numerical simulation, this study explored the characteristics and interactions of surface sensible heating and atmospheric latent heating over the main part of the Tibetan Plateau, i.e., terrain at elevations >2 km in summer. The impacts of these two types of heating on local vertical motion and monsoonal meridional circulation were compared. Theoretical analysis and numerical experimentation demonstrated that by changing the configuration of the upper-tropospheric air temperature and circulation, the two types of heating could generate both minimum absolute vorticity and abnormal potential vorticity forcing near the tropopause, enhance the meridional circulation of the Asian summer monsoon, and produce an eastward-propagating Rossby wave train within the mid-latitude westerly flow. Consequently, the manifestations of these features were shown to influence the circulation of the Northern Hemisphere.

Keywords Tibetan Plateau, Surface sensible heating, Latent heating, Monsoonal meridional circulation, Potential vorticity forcing

Citation: Wu G X, Zhuo H F, Wang Z Q, Liu Y M. 2016. Two types of summertime heating over the Asian large-scale orography and excitation of potential-vorticity forcing I. Over Tibetan Plateau. *Science China Earth Sciences*, 59: 1996–2008, doi: 10.1007/s11430-016-5328-2

1. Introduction

The Tibetan Plateau (TP) covers about 25% of the territory of China, with an average elevation of terrain of >4 km. The height of the topography around the TP, especially on its southern slope, increases rapidly. There is significant contrast between the western and eastern TP with regard to land surface features, vegetation, and meteorological characteristics (Ye and Gao, 1979). The mass of air above the TP is only about 60% of that above land at sea level. Moreover,

radiative processes over the TP are very different from the surrounding regions at lower elevations, especially within the atmospheric boundary layer (Smith and Shi, 1992; Liu et al., 2006). Thus, the thermal processes over the TP possess distinct features, and the TP exerts significant influence on the circulation systems, weather, and climate of the local and surrounding regions (and even the entire globe) through its distinct thermodynamic and mechanical effects (Yanai and Wu, 2006; Xu et al., 2008a, 2008b, 2010).

Previous studies have revealed the distribution features of heating over the TP by analyzing the sensible heating (SH) in summer or by back-computing the total heat source Q_1 (Luo and Yanai, 1984; Yanai et al., 1992; Yanai and Wu, 2006). According to the theory of the TP “SH-driven air

†Corresponding author (email: lym@lasg.iap.ac.cn)

*Corresponding author (email: wangziq5@mail.sysu.edu.cn)

pump" (TP-SHAP) (Wu et al., 1997, 2007), SH on the surface of the TP can drive low-level water vapor in surrounding regions to converge rapidly on the TP, resulting in considerable condensation and precipitation over the southern TP and northern parts of South Asia. However, the spatial distribution of precipitation over the southern slope of the TP is not uniform. Moreover, the water vapor conveyor belt along the Somali jet from the Southern Hemisphere also does not ascend uniformly over the southern slope of the TP. One branch of the conveyor belt deviates northward over the central Bay of Bengal. It then ascends over the southern slope of the TP, forming a center of heavy rainfall there in the summer. Conversely, less precipitation appears over the western TP. Therefore, summer heating over the TP should include two different types: surface SH and condensational latent heating (LH) that is affected by the SH. However, precipitation over the TP can regulate both the surface thermal balance and the SH. Therefore, to understand better the effects of the TP on the weather and climate, it is necessary and important to reveal the characteristics and interactions of these two different types of heating.

Many studies have shown that thermal forcing over the TP influences not only the variability of the precipitation of the South Asian monsoon (Wang, 2006), but also the precipitation of the East Asian monsoon (Chang, 2004), and even the global circulation. However, the details of the associated dynamic mechanisms remain unclear. In this study, the characteristics and interactions of the summertime surface SH and LH over the main part of the TP (main TP), i.e., terrain with elevation >2 km ($h>2$ km), was investigated using the Weather Research and Forecasting (WRF) model. The impacts of these two types of diabatic heating on local vertical motion and monsoonal meridional circulation were compared. To further the understanding of the mechanisms via which these two types of heating over the TP affect the weather and climate, their influences on the configuration of the temperature and the circulation in the upper troposphere (and the consequent formation of the strongest anticyclone there), and on the generation of potential vorticity forcing near the tropopause were also explored.

2. Model and experiment design

The WRF model version 3.4.1 (Skamarock et al., 2008) was used in this study. This model has been employed previously as a regional climate model to simulate variations of the Asian summer monsoon (e.g., Kim and Hong, 2010; Yang et al., 2012; Wang et al., 2014a). Compared with the atmospheric general circulation model, the WRF has greater resolution that can represent topography more accurately and incorporate land surface processes that are more reasonable. Therefore, it can be considered a useful tool in research into the effects of the TP on weather and climate. The physical packages incorporated in the WRF model for

this study included the WRF Single-Moment 6-Class microphysics scheme (Hong and Lim, 2006), Grell-Devenyi convective scheme (Grell and Devenyi, 2002), Noah land-surface model (Chen and Dudhia, 2001), BouLac planetary boundary layer scheme (Bougeault and Lacarrere, 1989), Goddard shortwave scheme (Chou and Suarez, 1999), and Rapid Radiative Transfer Model for longwave radiation (Mlawer et al., 1997). The simulation domain covered most parts of Asia and the adjacent oceans with 133 grid points latitudinally and 195 grid points longitudinally (a buffer zone had five grid points). A Lambert projection was adopted and the domain was centered at 30°N , 95°E (Figure 1a). The model has 45-km horizontal resolution and 35 vertical layers with a terrain-following sigma coordinate and a prescribed model top at 50 hPa. The initial state of the atmosphere and the lateral boundary conditions (updated every 6 h) were obtained from the Final Analysis of National Centers for Environmental Prediction (<http://rda.ucar.edu/datasets/ds083.2/>), and the sea surface temperature (SST) forcing dataset was the Optimum Interpolation SST (Reynolds et al., 2007) from the National Oceanic and Atmospheric Administration, which was updated daily.

Four ensemble experiments were performed and each incorporated six summers (2003–2008) with the initial conditions set at 0000 UTC May 1. The integration time was 4 months, i.e., every experiment ended at 1800 UTC August 31, and the output data derived from the final 3 months (June–August, JJA) were analyzed. Table 1 shows the details of the experiment design. The normal experiment with the WRF model was named the control run (CTL). Results obtained from the CTL were used for comparison with those obtained from the other sensitivity experiments. The CTL run reproduced the fields of both precipitation and wind vector at 850 hPa reasonably well compared with the TRMM satellite-observed precipitation and the 850-hPa wind derived from the National Centers for Environmental Prediction reanalysis (Figure 1b and 1c). The distributions of the summer monsoon circulation and precipitation over the Arabian Sea, Bay of Bengal, South China Sea, southern TP, and East Asia were all simulated well, indicating that the CTL run could serve as the background experiment of the summer monsoon. Figure 2a and 2b show the spatial distributions of the JJA average surface SH and condensational LH over the TP and its surrounding areas in the CTL. In agreement with the precipitation shown in Figure 1c, the LH center is located over the southern slope and southeastern areas of the TP with a maximum value of >300 W m^{-2} , which decreases northwestward to <30 W m^{-2} . In contrast, SH is weakest (<40 W m^{-2}) over the southeastern TP but strongest (>100 W m^{-2}) over the northwestern TP. This indicates that over the TP, SH is generally weaker than LH and the SH distribution is influenced by LH.

Previous studies have usually focused on the weather and climatic effects of the entire TP. The purpose of this study was to reveal the different features and effects of surface SH

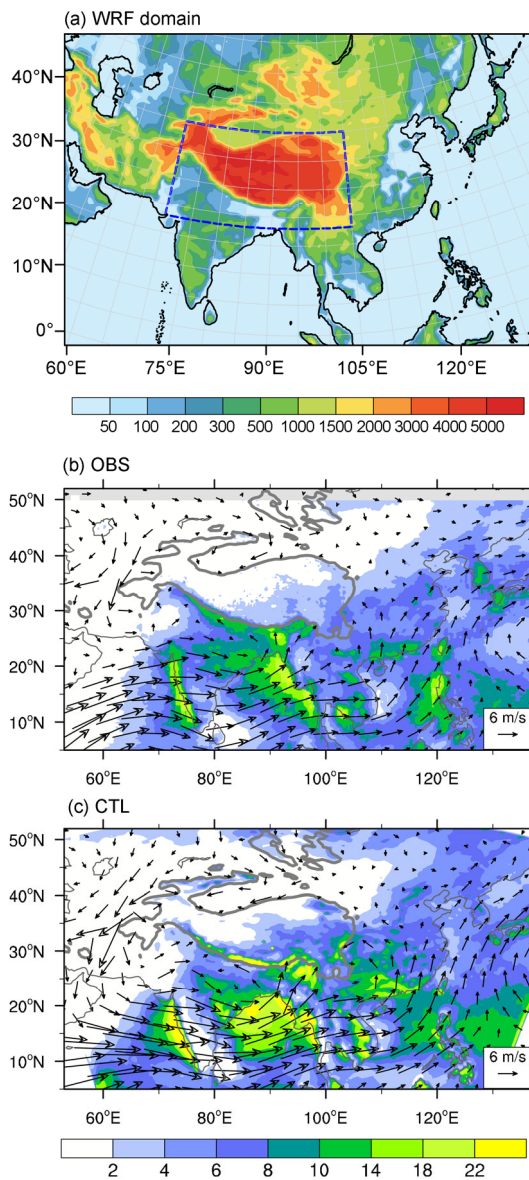


Figure 1 (a) Selected domain of the WRF model used for the sensitivity experiments (blue dashed line) and the elevation of orography (m), (b) precipitation retrieved from TRMM (shading, mm d⁻¹) and the wind at 850 hPa (vector, m s⁻¹) from NCEP-FNL reanalysis, and (c) the same as (b) except from the CTL experiment. The heavy gray curve in (b) and (c) denotes the 2-km contour of topography.

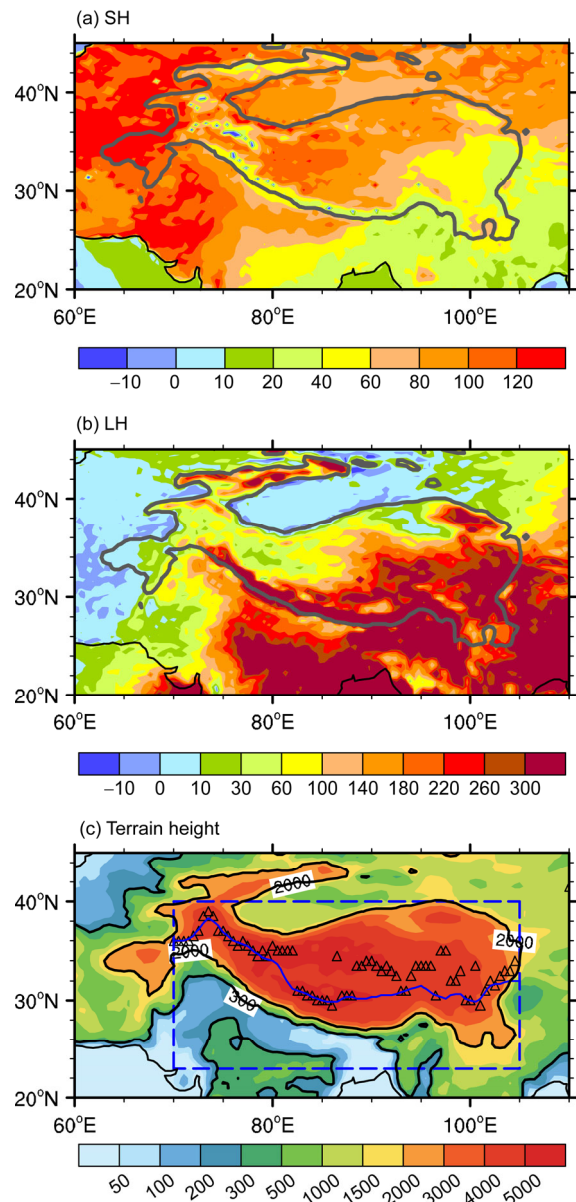


Figure 2 Simulated surface sensible heating (W m⁻²) (a) and latent heating (W m⁻²) (b) in the CTL experiment. (c) Experiment design for the STP_NS run and elevation (m). The black triangle denotes the location of the highest elevation along the same latitude, and the blue solid contour indicates the northern boundary of the southern slope of the TP in the STP_NS experiment.

Table 1 Details of experiment description

Experiment title	Experiment description
CTL	Back ground, climate mean
TP_NL	No latent heating over the main part of the TP ($h > 2$ km)
TP_NS	No surface sensible heating over the main part of the TP ($h > 2$ km)
STP_NS	No surface sensible heating over the southern slope of the TP

and convective LH over the main TP. Thus, the region for performing the sensitivity experiments was defined as those

model grids where terrain is > 2 km over the main TP (23°–40°N, 70°–105°E). Different from the CTL, one sensitivity experiment (TP_NL) was designed to illustrate the effects of condensational LH on the Asian monsoon, in which the LH of the entire vertical atmospheric column over the main TP was removed. In another sensitivity experiment (TP_NS), the surface SH released over the experimental area was not allowed to heat the atmosphere. Additionally, to investigate the feedback process between SH and precipitation over the southern slope of the TP, a third sensitivity experiment (STP_NS) was added. STP_NS was

similar to the TP_NS experiment, but only the surface SH over the southern slope of the TP was not allowed to heat the atmosphere. The southern slope of the TP was defined as those grid points north of 23°N and between 70° and 105°E, where topography is higher than 300 m and lower than the maximum elevation at the same longitude of the grid point. If the maximum elevation was located within the central TP to the north of the Himalayas, then the next maximum elevation to its south was chosen. The resultant northern border of this southern slope is shown in Figure 1c, indicated by the blue contour.

3. Two types of diabatic heating over the main TP and their interaction

3.1 Effects of surface sensible heating (SH)

Figure 3a presents the precipitation and near-surface wind at $\sigma=0.98$ in the TP_NS experiment. Without surface SH, an anticyclonic circulation appears on the TP surface, forming divergence and descent of air to its south near the southeastern boundary of the plateau. This is in distinct contrast with the convergence and ascent of air at 850 hPa in the same region in the CTL run (Figure 1c). The distributions of precipitation and circulation beyond the plateau region in this experiment differ little from those in the CTL run. It is worth noting that in the TP_NS experiment, surface SH is removed only in the main TP area where elevation $h>2$ km. In an experiment in which the surface SH was removed across the entire TP area, including the area with elevation $h<2$ km, the precipitation over the Indochina Peninsula and East Asia decreases substantially (Wu et al., 2012). We can thus infer that the impact of the TP on the precipitation of the Asian summer monsoon is mainly attributable to surface SH over its lower slopes where $h<2$ km. This is because, following potential vorticity theory, surface SH over its lower slopes can generate near-surface cyclonic circulation that can transport substantial quantities of water vapor from the sea to the land area, forming continental monsoonal precipitation (He et al., 2015). Although surface SH over the main TP ($h>2$ km) can also produce cyclonic circulation (Figure 3b), it generates much less water vapor transport there and its contribution to monsoonal precipitation in the surrounding area becomes much weaker.

To a certain extent, the difference between the CTL and TP_NS runs represents the effect of surface SH over the main TP. Such an effect forms a prominent surface cyclonic convergent circulation, which is centered over the TP, with air converging from the lower surface of the TP (including its surrounding area) toward its higher elevation (Figure 3b). The surface SH on the main TP also leads to increased precipitation over the central, eastern, and southern plateau with a maximum of more than 6 mm d⁻¹ over the southeastern TP. Precipitation also increases over East Asia and the Bay of Bengal but it decreases over the tropical continent in

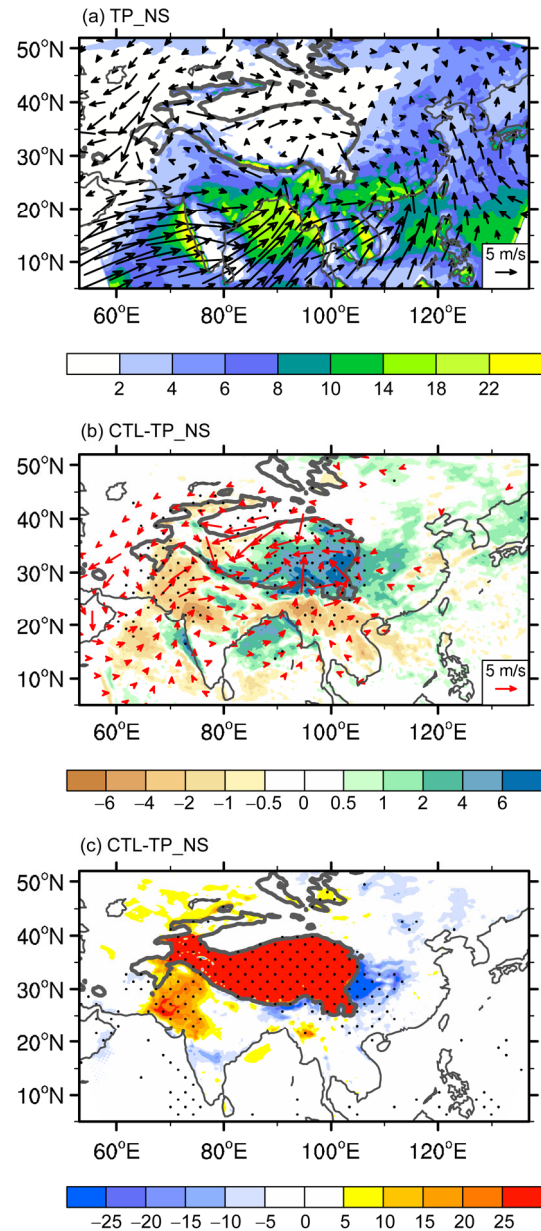


Figure 3 Mean summer precipitation (shading, unit: mm day⁻¹) and surface flow at the $\sigma=0.98$ level (vectors, m s⁻¹) for (a) the TP_NS experiment and (b) the difference between CTL and TP_NS. (c) The same as (b) but for the surface sensible heating (unit: W m⁻²). Dotted regions in (b) and (c) denote statistical significance above the 95% level. Only the wind differences with statistical significance above the 95% level are plotted in (b).

South Asia. Because of the difference in precipitation, surface SH beyond the TP area also changes (Figure 3c); it increases over northwestern India where precipitation is decreased and it decreases over the southern border of the TP and to its east where precipitation is increased.

3.2 Effects of convective latent heating (LH)

In the TP_NL experiment, in which the LH over the main TP was removed, the distributions of precipitation and surface

circulation in the area beyond the TP (Figure 4a) change little in comparison with the distribution of precipitation and wind at 850 hPa in the CTL run (Figure 1c). The results are similar to those achieved in the experiment without surface SH (i.e., TP_NS), as shown in Figure 3a. What is different is the existence of surface SH in the TP_NL run. Consequently, surface cyclonic circulation develops over the TP accompanied by surface convergence and strong precipitation

of $>4-6 \text{ mm d}^{-1}$.

To a certain extent, the difference between the CTL and TP_NL runs represents the effect of convective LH over the main TP. Beyond the TP area, such an effect also increases precipitation over the Bay of Bengal and East Asia and it decreases precipitation over continental in South Asia (Figure 4b), similar to the results obtained in the SH case (Figure 3b). These results are also close to the findings obtained from data analysis (Zhao and Chen, 2001; Zhou et al., 2009) and from other sensitivity experiments (Wang et al., 2014b; Wu et al., 2015a). The agreement between the results from observations and experiments is because the atmospheric response to diabatic heating over the TP is subject to the potential vorticity constraint and to atmospheric thermal adaptation (Wu and Liu, 2000; Wu et al., 20015a). Within the TP area, such an effect increases precipitation in the north and reduces it in the south, in good agreement with the west-east-oriented convergent zone in the surface wind field that is located over the southern TP. The difference in the distribution of precipitation has a strong impact on the distribution of surface SH (Figure 4c); it decreases in the southern TP where precipitation is increased and it increases in the north where rainfall is reduced.

The aforementioned association between precipitation and SH is not a single-direction cause-effect relation. To understand their complex interaction and feedback, another numerical experiment (STP_NS) was designed in which the surface SH over the southern slope of the TP was removed, as shown in Figure 2c. The differences in the results can be considered the consequence of the effect of surface SH on the southern slope of the TP, and they can be used for comparison with the results induced by diabatic heating over the TP. The differences in precipitation and wind field at 850 hPa are presented in Figure 5.

The effects induced by surface SH on the southern slope of the TP (Figure 5a) are similar to those induced by LH over the main TP (Figure 5c). For example, they both form cyclonic circulation at 850 hPa surrounding the TP, increase precipitation over East Asia and the Bay of Bengal, decrease precipitation over the tropical continent, and cause increasing rainfall over the southern TP and decreasing rainfall over its north. Despite these similarities, the difference in precipitation presented in Figure 5a is a consequence of the surface SH over the southern slope of the TP, whereas the precipitation difference presented in Figure 5c leads to the decreased surface SH in the south and increased surface SH in the north of the TP (Figure 4c). This indicates that surface SH over the southern slope of the TP can result in increased precipitation over the southern TP. Conversely, increased precipitation over the southern TP can weaken surface SH over the southern slope, leading to reduced local precipitation. We can thus infer that precipitation (LH) and surface SH over the TP interact strongly and that their distributions, as observed either in the real atmosphere or in a numerical model, represent the quasi-equilibrium state of

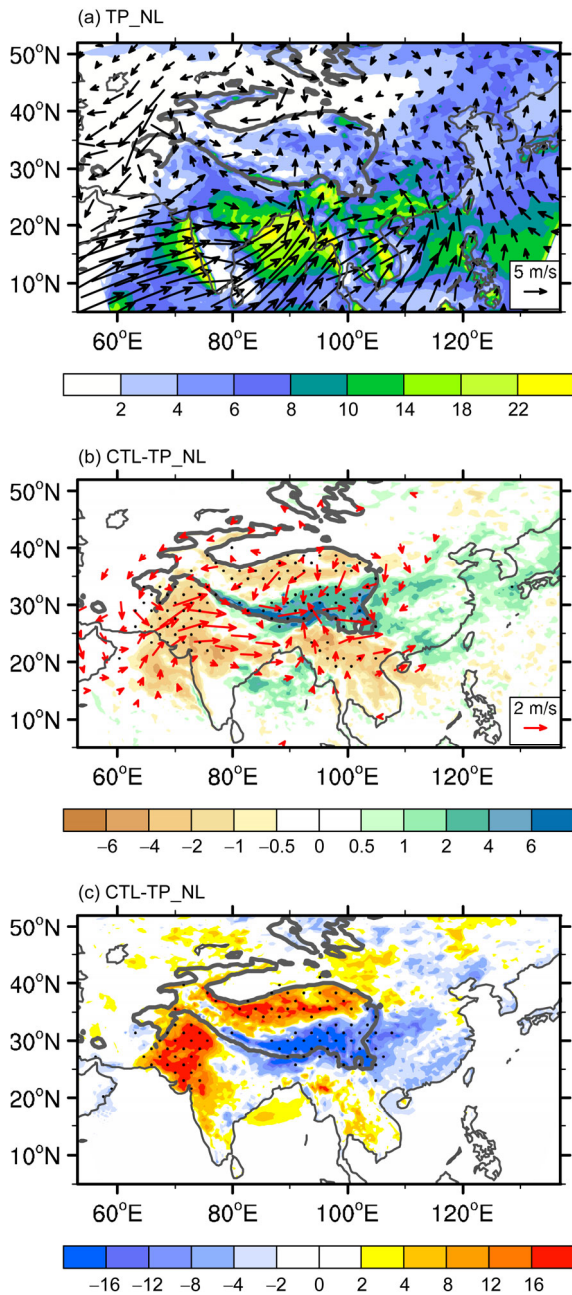


Figure 4 Mean summer precipitation (shading, unit: mm day^{-1}) and surface flow at the $\sigma=0.98$ level (vectors, m s^{-1}) for (a) the TP_NL experiment and (b) the difference between CTL and TP_NL. (c) The same as (b) but for the surface sensible heating (unit: W m^{-2}). Dotted regions in (b) and (c) denote statistical significance above the 95% level. Only the wind differences with statistical significance above the 95% level are plotted in (b).

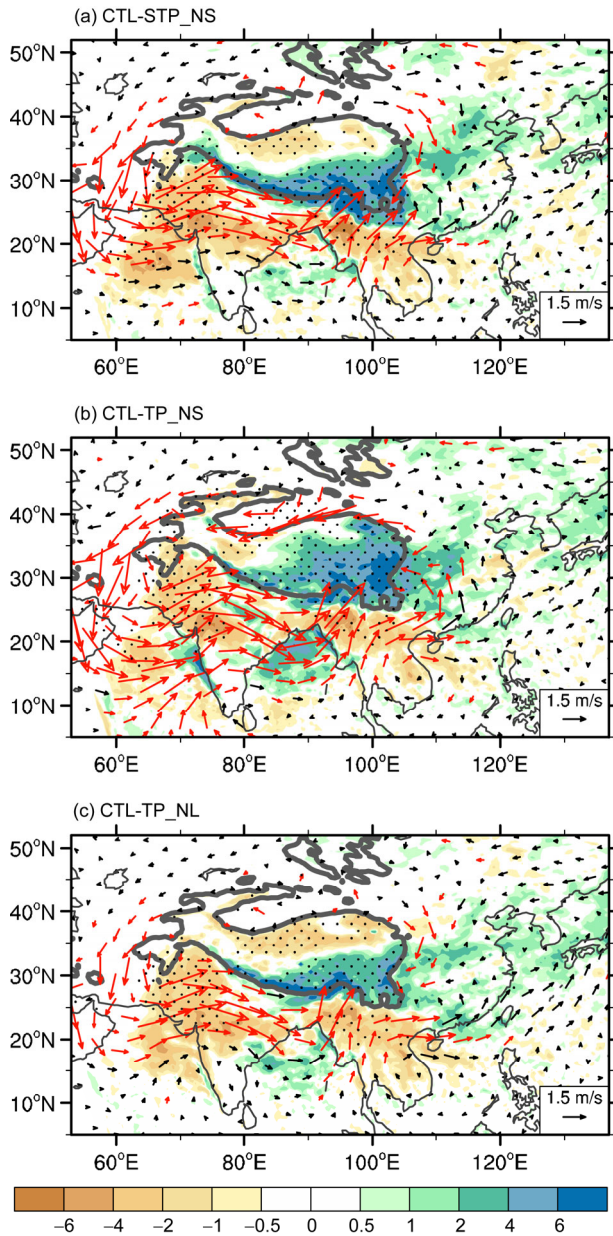


Figure 5 Differences in mean summer precipitation (shading, unit: mm day^{-1}) and 850-hPa wind (vectors, unit: m s^{-1}) between CTL and STP_NS (a), CTL and TP_NS (b), and CTL and TP_NL runs (c). Dotted regions denote the statistical significance of precipitation anomalies is above the 95% level. Wind differences significant above the 95% level are plotted in red.

such a complex interaction and feedback mechanism. When surface SH exists over the entire TP (Figure 5b), although the distributions of both circulation and precipitation are similar to those presented in Figure 5a and 5c, their intensities are remarkably intensified. Comparison between Figure 5a and 5b also demonstrates that the increase of surface SH over the northern TP can intensify considerably the atmospheric convergence from the surrounding areas toward the TP, leading to the prominent increases of precipitation and LH over the central TP.

4. Effects on local meridional circulation

Figure 6 shows the distribution of the meridional circulation, averaged for the longitudinal domain $85^{\circ}\text{--}95^{\circ}\text{E}$ over the Bay of Bengal, in the different experiments and their differences from the CTL run. In the CTL experiment (Figure 6a), two distinct branches of upward motion are located between the equator and 20°N , and over the southern slope of the TP. These correspond to the southern and northern branches of the South Asia summer monsoon, respectively (Wu et al., 2012). The upward motion of the southern branch changes little in the TP_NS and TP_NL experiments (Figure 6b and 6c, respectively); however, the upward motion of the northern branch weakens considerably or even disappears. Without surface SH, subsidence prevails over the TP (Figure 6b). Without LH, air ascent prevails over the northern TP with its maximum located near the surface (Figure 6c). This is because surface SH exists in the TP_NL experiment and surface convergence is strong (Figure 4a). Figure 6d demonstrates that surface SH significantly enhances air ascent over the entire TP and the region to its south. Conversely, LH over the main TP increases air ascent only over the southern TP and its southern slope (Figure 6e), while air descent occurs at 24°N and over the northern TP; the latter corresponds to reduced precipitation (Figure 4b) and increased surface SH (Figure 4c) in the area.

Scrutinizing the distribution of differences indicates that either the surface SH or the LH over the main TP can significantly enhance air ascent and induce southerly flow below 2 km to the south of the TP, leading to the increased precipitation over the southern slope of the TP (Figure 5b and 5c). However, SH has greater influence (Figure 6d) than LH (Figure 6e). This is because strong surface SH over the southern slope (where $h > 2$ km) in the sensible heat experiment can induce stronger ascent of air along the upper slope, generating stronger pumping on flow of the lower-level air. In both the CTL and the TP_NL experiments, surface SH exists over the southern slope; however, precipitation over the southern slope in the CTL run is $>10 \text{ mm d}^{-1}$ (Figure 1c). Consequently, the difference in SH over the southern slope between the two experiments is not great and it even becomes negative. Thus, the pumping effect on the lower atmosphere as a result of air ascent cannot be reinforced by surface SH along the slope, and it even becomes much weaker than the pumping due to the surface SH over the main TP. Actually, because the surface SH on the main TP can produce precipitation over the main TP (Figure 5b), generating LH over the main TP, it is unsurprising that the pumping effect due to SH over the TP is stronger than that due to LH.

5. Effects on temperature and circulation in the upper troposphere

During summer, the distributions of temperature and diabatic

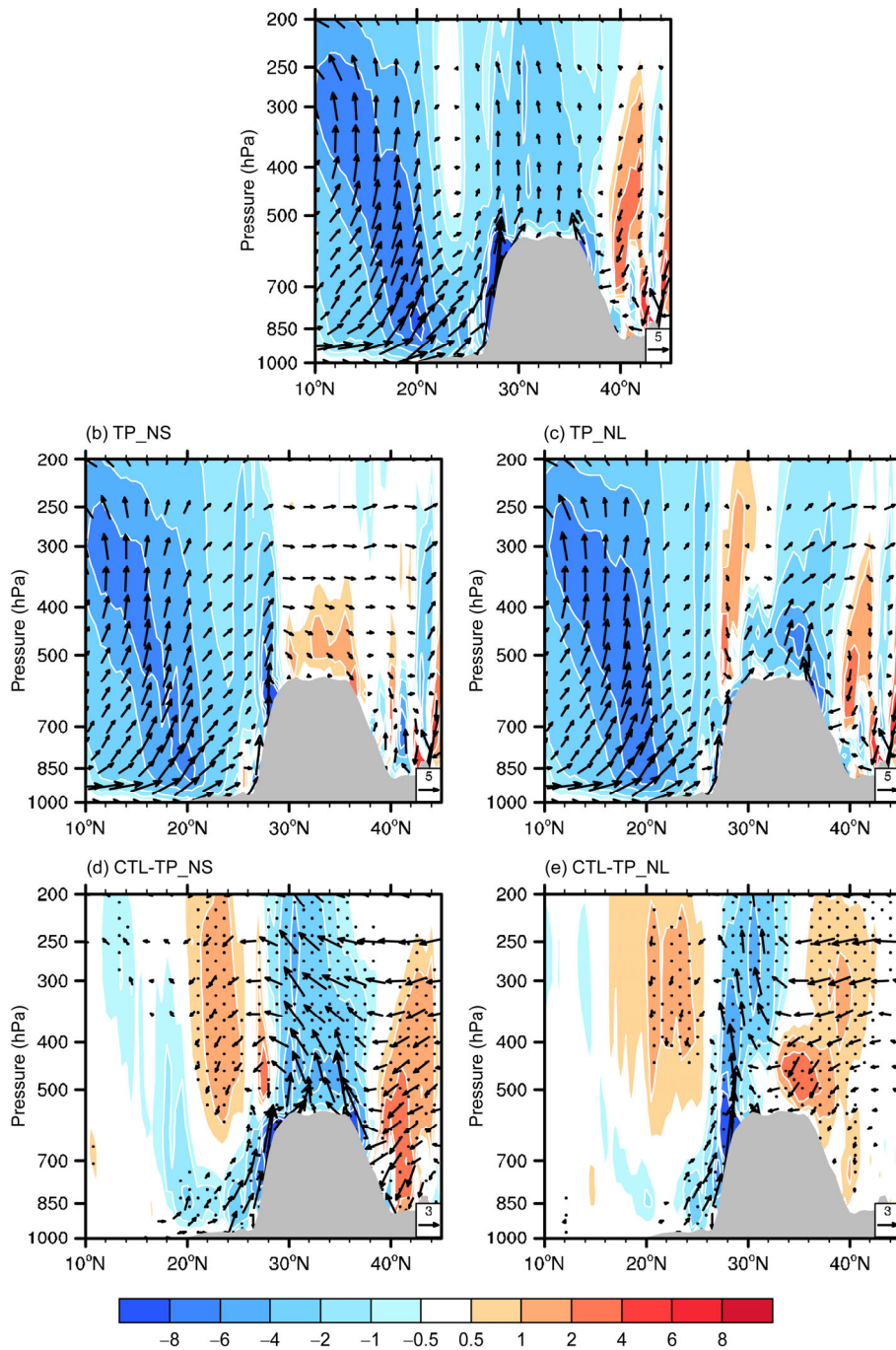


Figure 6 Pressure–latitude cross sections of the vertical circulation (vectors, v and $-50*\omega$) and vertical velocity (shading, unit: 0.02 Pa s^{-1}) averaged from 85°E to 95°E for the experiments of CTL (a), TP_NS (b), and TP_NL (c), and the differences between CTL and TP_NS (d) and CTL and TP_NL (e). Dotted regions in (d) and (e) denote statistical significance of vertical velocity differences above the 95% level. Only vertical circulation differences in (d) and (e) with statistical significance above the 95% level are plotted.

heating in the upper troposphere satisfy the following $T-Q_z$ distribution (Wu et al., 2015b):

$$T(x) \approx \lambda \partial Q(x) / \partial x,$$

in which

$$\lambda = \left(\frac{L}{H_Q} \right)^2 \frac{H}{R\beta\theta_z} f(f + \zeta),$$

where L and H_Q denote the zonal and vertical scales of temperature and heating respectively, θ_z is the vertical gradient of potential temperature, and the other parameters are variables normally used in atmospheric science. The above $T-Q_z$ relation implies that the warm/high pressure center in the upper troposphere between 200 and 400 hPa should be located to the west of a heating region and to the east of a

cooling region.

The distributions of temperature and wind at 300 hPa in the different experiments are presented in Figure 7a–7c. The warm anticyclonic circulation in the CTL run is stronger and it covers a wider area than that in either the TP_NS or the TP_NL experiments. The warm center in the CTL run is located at 27°N, 80°E, which is to the west of the region of heavy precipitation (Figure 1c) and close to the observations; however, it is located to the south of 25°N, i.e., beyond the TP, in the experiments without either SH or LH over the main TP. The difference in the distributions shown in Figure 7d and 7e demonstrate that diabatic heating of the main TP not only intensifies the warm anticyclone but it also shifts its center northwestward, resulting in downstream energy dispersion and the formation of a cold cyclonic cir-

ulation in the region of Mongolia and Northeast China. It is noteworthy to highlight that these warm centers are located to the west of the corresponding precipitation centers (Figure 5b and 5c), which is in agreement with the $T-Q_z$ relation, implying that the variation of the upper tropospheric warm center is a consequence of the difference in LH induced by diabatic heating over the main TP. A comparison of Figure 7d and 7e reveals that surface SH over the main TP has much greater effect than LH on the intensification of the warm anticyclone over South Asia. This is because, as discussed above, surface SH on the main TP can trigger and enhance LH over the TP (Figure 3b), which intensifies the total diabatic heating over the TP. However, LH over the main TP reduces considerably the surface SH over the southern slope of the TP (Figure 4c) such that the

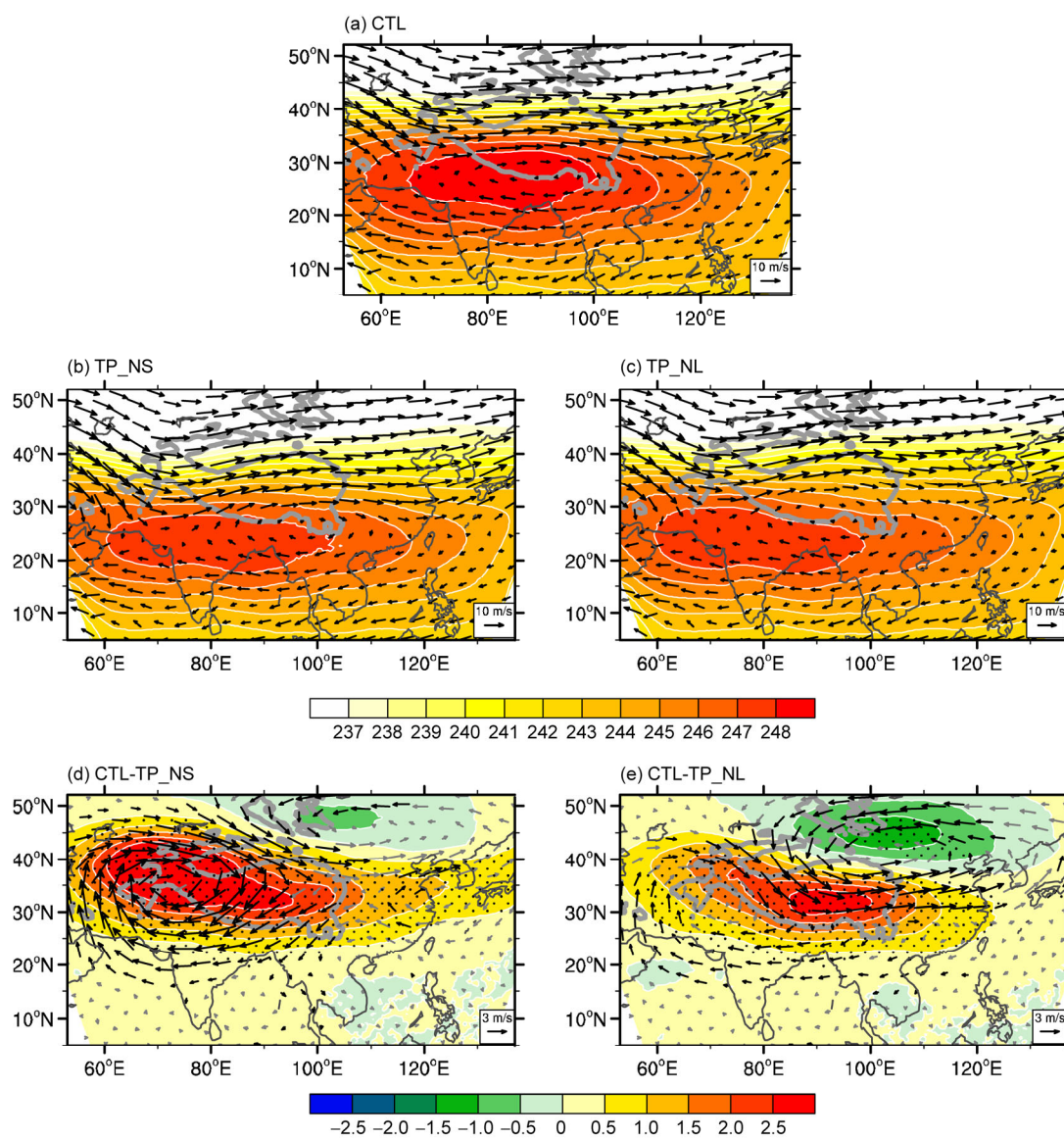


Figure 7 Mean summer air temperature (shading, unit: K) and wind field (vectors, unit: m s^{-1}) at the 300-hPa level for the experiments of CTL (a), TP_NS (b), and TP_NL (c), CTL minus TP_NS (d), and CTL minus TP_NL (e). Dotted regions in (d) and (e) denote statistical significance of temperature anomalies above the 95% level. Wind differences in (d) and (e) significant above the 95% level are plotted in black.

total heating of the TP is weaker.

The distributions of temperature and wind at 100 hPa in the different experiments are presented in Figure 8a–c. At this level, the South Asian anticyclonic circulation is similar to that at 300 hPa. However, the distribution of temperature is changed completely. The warm center over South Asia disappears and the temperature increases polewards. This is because the 100-hPa surface is located within the upper troposphere in the tropics, which is where the air is cold, whereas it is located within the stratosphere in the mid-high latitudes.

The difference in the circulation at the 100-hPa level (Figure 8d and 8e) is similar to that at 300 hPa but the intensity is greatly intensified. Most importantly, this 100-hPa anticyclonic center has a cold core, which contrasts with the warm feature of the anticyclone at 300 hPa. This implies

that diabatic heating over the main TP can have considerable influence on the spatial configurations of temperature and circulation near the tropopause.

6. Diabatic heating over the TP and potential vorticity forcing near the tropopause

Figures 7d, 7e, 8d, and 8e show the differences in the temperature and circulation in the upper troposphere and lower stratosphere between the experiments with and without TP diabatic heating. In the following, we consider the significance of diabatic heating of the TP on weather and climate by analyzing both the similarities of the differences in circulation and the contrasts of the differences in temperature between 100 and 300 hPa, as excited by TP thermal forcing.

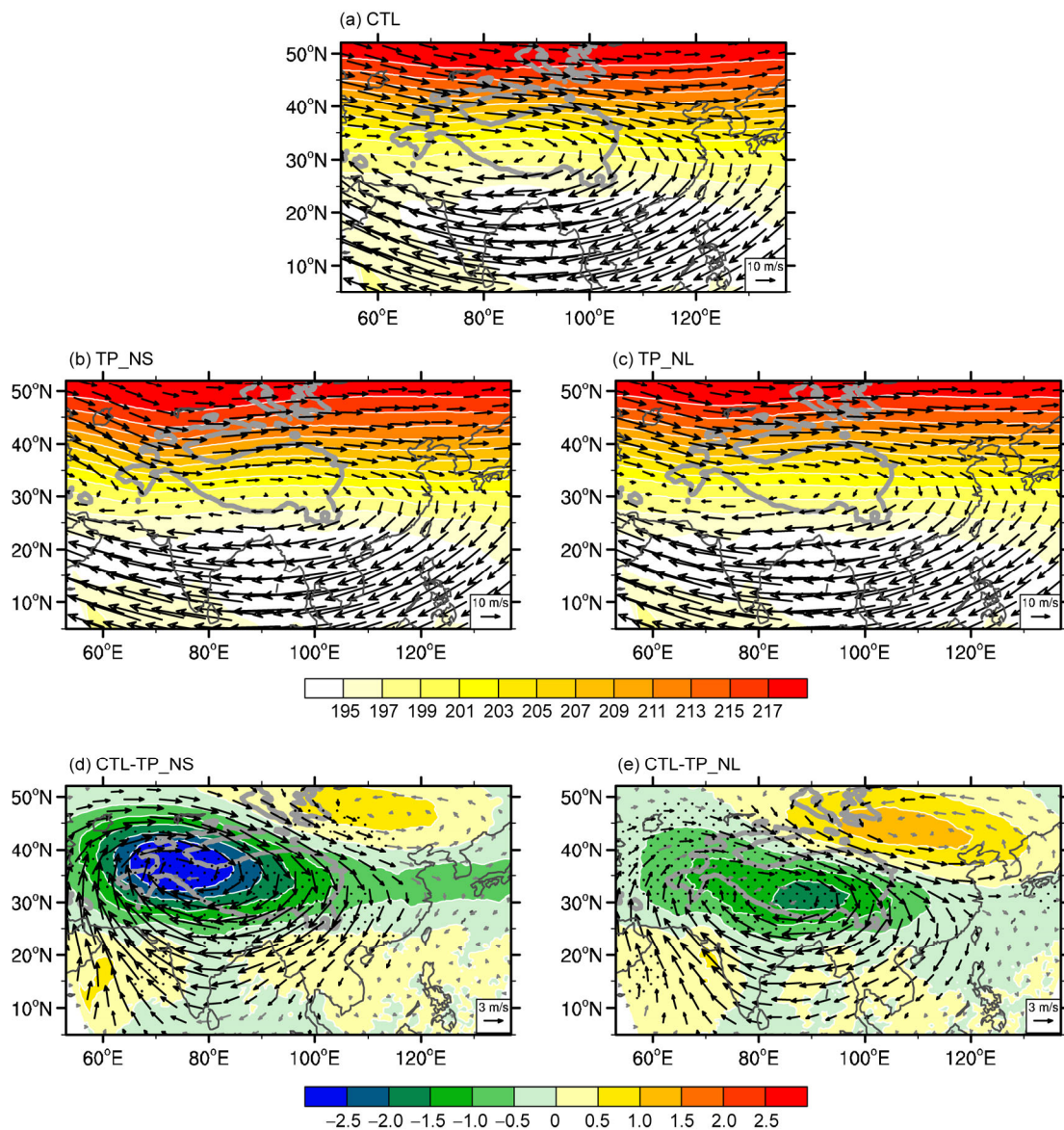


Figure 8 As in Figure 7, but for the air temperature (shading, unit: K) and wind field (vectors, unit: m s^{-1}) at the 100-hPa level.

6.1 Existence of a maximum anticyclonic circulation near the tropopause

Suppose there exist a level p_c between 100 and 300 hPa, i.e.:

$$p_c(x, y), 100 \text{ hPa} < p_c < 300 \text{ hPa}.$$

The upper-layer anticyclone is cold above, warm below, and neutral at p_c :

$$\nabla_p T \equiv 0, p = p_c(x, y). \quad (1)$$

We first prove that this neutral anticyclone is the strongest anticyclone in the upper troposphere. In a polar coordinate system, the thermal wind relation can be written as

$$\frac{\partial v_s}{\partial \ln p} = -\frac{R}{f} \frac{\partial T}{\partial \gamma}, \quad (2)$$

or as

$$\frac{\partial v_s}{\partial p} = -\frac{R}{fp} \frac{\partial T}{\partial \gamma}, \quad (3)$$

where γ denotes the radial distance and v_s is the tangential wind, which is positive when the wind is anticlockwise in the Northern Hemisphere. Because at the p_c level, $\frac{\partial T}{\partial \gamma} \equiv 0$,

following the thermal wind relation (3): $\frac{\partial v_s}{\partial p} = 0$. Thus, the

circulation obtains its maximum at the level p_c . Differentiating both sides of eq. (3) with respect to pressure p leads to:

$$\frac{\partial^2 v_s}{\partial p^2} = \frac{R}{fp^2} \frac{\partial T}{\partial \gamma} - \frac{R}{fp} \frac{\partial}{\partial \gamma} \left(\frac{\partial T}{\partial p} \right). \quad (4)$$

Because following eq. (1), $\frac{\partial T}{\partial \gamma} \equiv 0$, at $p=p_c$, we get:

$$\frac{\partial^2 v_s}{\partial p^2} = -\frac{R}{fp} \frac{\partial}{\partial \gamma} \left(\frac{\partial T}{\partial p} \right), p=p_c. \quad (5)$$

From Figures 7d, 7e, 8d, 8e, and 9, near the center ($r \rightarrow 0$) and near the boundary ($r \rightarrow r_b$) of the difference anticyclone in the upper troposphere, the temperature increases from 100 to 300 hPa, satisfying the following conditions:

$$\begin{cases} \frac{\partial T}{\partial p} \gg 0, & r \rightarrow 0; \\ \frac{\partial T}{\partial p} > 0, & r \rightarrow r_b. \end{cases}$$

Substituting the above into eq. (5) leads to:

$$\frac{\partial^2 v_s}{\partial p^2} > 0, p=p_c. \quad (6)$$

Therefore, from eqs. (3) and (6), we have proved that the tangential wind speed reaches its minimum at the p_c level in the vertical direction, i.e., the anticyclonic circulation at the level $p=p_c$ is the strongest anticyclone in the upper troposphere (100–300 hPa).

The existence of a strong anticyclone in the upper troposphere provides important dynamic conditions for the development of the local monsoonal meridional circulation. This is because the response of the atmospheric meridional circulation to axisymmetric heating possesses two distinct types of circulation: the thermal equilibrium (TE) type and the angular momentum conservation (AMC) type (Schneider, 1977, 1987; Schneider and Lindzen, 1977; Held and Hou, 1980). Based on the dynamic equation set, Plumb and Hou (1992) derived the transformation criteria between the TE and AMC (their eqs. (7) and (8)). In the mid-high latitudes, atmospheric inertial stability is strong and the response obtains a TE-type solution. In the tropics and subtropics, when absolute vorticity becomes small or even negative, the criteria deviate and the response obtains an AMC-type solution, and the monsoonal meridional circulation can develop easily. Figure 10 shows the distributions of absolute vorticity at 150 hPa in the different experiments and their differences compared with the CTL run. The results demonstrate that either surface SH or LH over the main TP can reduce the absolute vorticity above the TP by more than $2 \times 10^{-5} \text{ s}^{-1}$ (Figure 10d and 10e), forming a region of minimum absolute vorticity just over the TP (Figure 10a). This helps the excitation of the monsoonal meridional circulation to the south of the TP (Figure 6d and 6e) in conjunction with the northern branch of the South Asian summer monsoon. These results indicate that the existence of the strongest anticyclone circulation at the $p=p_c$ level, induced by TP thermal forcing, provides important conditions necessary for the development of the meridional circulation in the Asian monsoon area.

6.2 Location of strongest anticyclone circulation is near the tropopause

From Figures 7 and 8, the thermal configuration of the

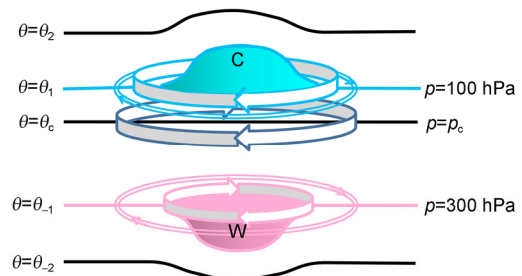


Figure 9 Schematic indicating the formation of the area of minimum PV forcing near the tropopause due to thermal forcing over the main TP. Vector indicates anticyclonic circulation; “C” and blue color denotes cold temperature, and “W” and pink color denotes warm temperature.

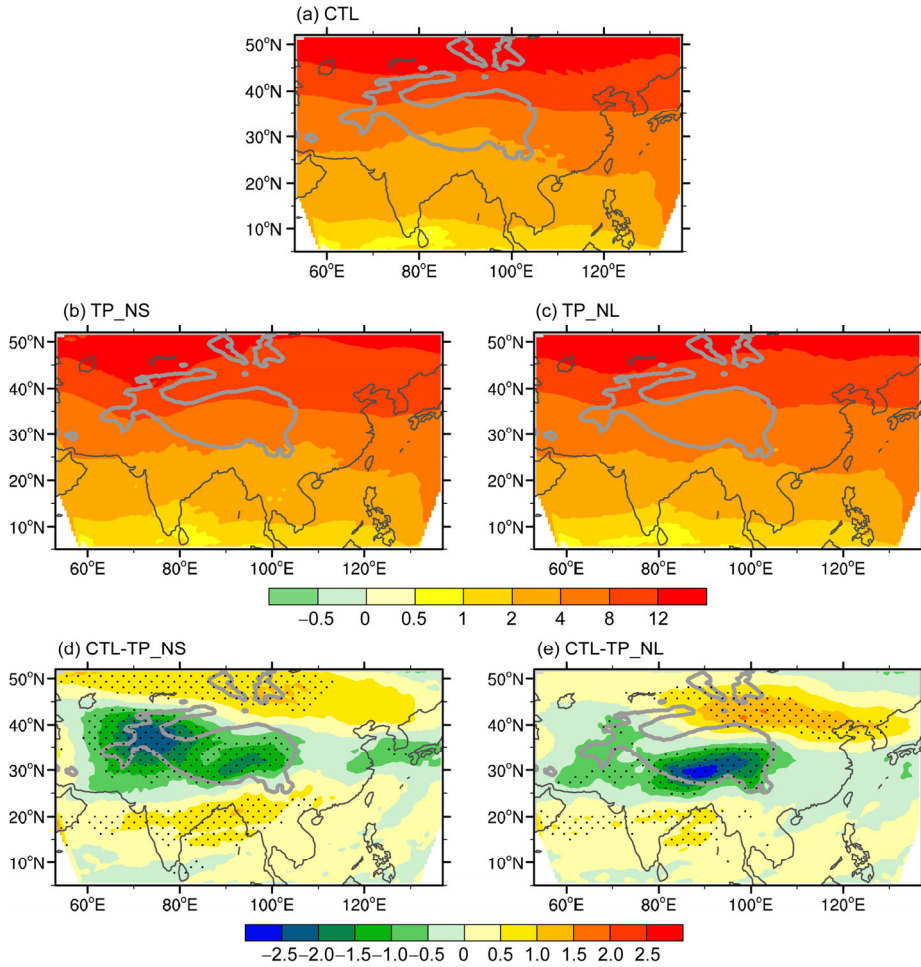


Figure 10 Mean summer distribution of absolute vorticity (shading, unit: 10^{-5} s^{-1}) at the 150-hPa level for the experiments of CTL (a), TP_NS (b), TP_NL (c), CTL minus TP_NS (d), and CTL minus TP_NL (e). Dotted regions in (d) and (e) denote statistical significance of the difference above the 95% level.

anticyclone in the upper troposphere can be constructed and it is presented in Figure 9. The anticyclone is warm from the $p=p_c$ level downward and its intensity decreases downward according to (2). The anticyclone is cold from the $p=p_c$ level upward and its intensity should decrease upward as well, following the same argument. In addition, from eq. (3), we have:

$$\Delta v_s = -\frac{R\Delta p}{f p} \frac{\partial T}{\partial \gamma}. \quad (7)$$

This implies that the upward or downward vertical rate of decrease of the anticyclone at $p=p_c$ is proportional to the vertical distance Δp from p_c and to the horizontal temperature gradient $\partial T/\partial \gamma$, but it is inversely proportional to the atmospheric pressure p . Comparing Figure 7d with Figure 8d reveals that the temperature difference between the anticyclone center at 35°N, 75°E and its border at 35°N, 105°E is about 2°C at both 300 and 100 hPa, which indicates similarity of the horizontal temperature gradient $|\partial T/\partial \gamma|$ within the anticyclone at 300 and 100 hPa. According to (3), away

from the $p=p_c$ level, the downward rate of decrease of intensity $(\partial v_s/\partial p)_d$ is slower than the upward rate of decrease $(\partial v_s/\partial p)_u$. In other words, the warm anticyclone in the upper troposphere is a relatively deeper system, whereas the cold anticyclone aloft is shallower.

Assuming the tangential wind speed decreases downward from $p=p_c$ to 300 hPa by $(\Delta v_s)_d$, and upward from p_c to 100 hPa by $(\Delta v_s)_u$, then from eq. (7), we get:

$$\left| \frac{(p_c - 100)}{(300 - p_c)} \right| \propto \frac{(100 + p_c)}{(300 + p_c)} \cdot \left| \frac{(\Delta v_s)_u}{(\Delta v_s)_d} \right| \cdot \left| \frac{(\partial T/\partial r)_d}{(\partial T/\partial r)_u} \right|. \quad (8)$$

Because the anticyclone is stronger at 100 hPa than at 300 hPa, then

$$\left| \frac{(\Delta v_s)_u}{(\Delta v_s)_d} \right| < 1.$$

As

$$\left| \frac{(\partial T/\partial r)_d}{(\partial T/\partial r)_u} \right| \approx 1,$$

then

$$(p_c - 100) \ll (300 - p_c). \quad (9)$$

Therefore, the strongest anticyclone must be located at the $p=p_c$ level, which is very close to 100 hPa near the tropopause, i.e., the diabatic heating of the main TP in summer can induce the strongest anticyclonic circulation near the tropopause.

6.3 Minimum potential vorticity forcing near the tropopause

Importantly, the thermal characteristics of the anticyclone (i.e., cold aloft and warm below) cause the *in situ* static stability $\partial\theta/\partial z$ to become a minimum, such that the potential vorticity per unit mass at the anticyclonic center becomes a minimum, i. e.:

$$P = \alpha(f + \zeta) \frac{\partial\theta}{\partial z} = \text{Minimum}, p=p_c. \quad (10)$$

Figure 11 presents the longitude–height cross sections of the potential vorticity difference between the CTL run and the two sensitivity experiments. The latitude chosen for producing the cross section is along the latitude where the difference anticyclone center is located (refer to Figures 8d, 8e, 10d, and 10e). It shows that either surface SH or LH over the main TP can generate a center of minimum potential vorticity forcing at the level close to the tropopause (100–150 hPa). Compared with that induced by LH (Figure 11b), the center of minimum potential vorticity forcing induced by surface SH (Figure 11a) is located further westward and northward, and it is much stronger, with a maximum intensity of >1.2 PVU ($1 \text{ PVU} = 10^{-6} \text{ K m}^2 \text{ s}^{-1} \text{ kg}^{-1}$). Because this forcing center is located within the westerly flow, it can trigger a downward-propagating Rossby wave

train, as presented in Figures 7d, 7e, 8d, and 8e. It is evident that diabatic heating of the main TP can change the configuration of temperature and circulation in the upper troposphere and generate a source of minimum potential vorticity forcing near the tropopause and within the westerly flow, which influences the circulation and climate in the Northern Hemisphere.

7. Discussion and conclusions

Based on numerical modeling, this study investigated the characteristics and interactions of surface SH and LH in summer over the main TP with an elevation >2 km. Their impacts on vertical motion and the local monsoonal meridional circulation were analyzed, and their influences on the temperature and circulation of the upper atmosphere over the monsoonal area were highlighted.

The results demonstrated that surface SH of the TP can generate convective precipitation over the TP and produce LH, whereas LH over the TP can increase (decrease) precipitation over the southern (northern) TP and reduce (increase) the *in situ* surface SH. This indicates the existence of a feedback or interaction process between the two types of diabatic heating.

Surface SH over the main TP can generate ascent of air over the TP and regions to its south, significantly intensifying the southerly flow in the lower layer and the northerly flow aloft in the area of the Asian monsoon, such that the local monsoonal meridional circulation is enhanced. However, LH over the TP can produce an ascent of air over the southern TP and a descent of air over the northern TP and thus, its influence on the monsoonal meridional circulation is weaker.

Both SH and LH over the TP can enhance the warm center in the upper troposphere and the anticyclonic circulation

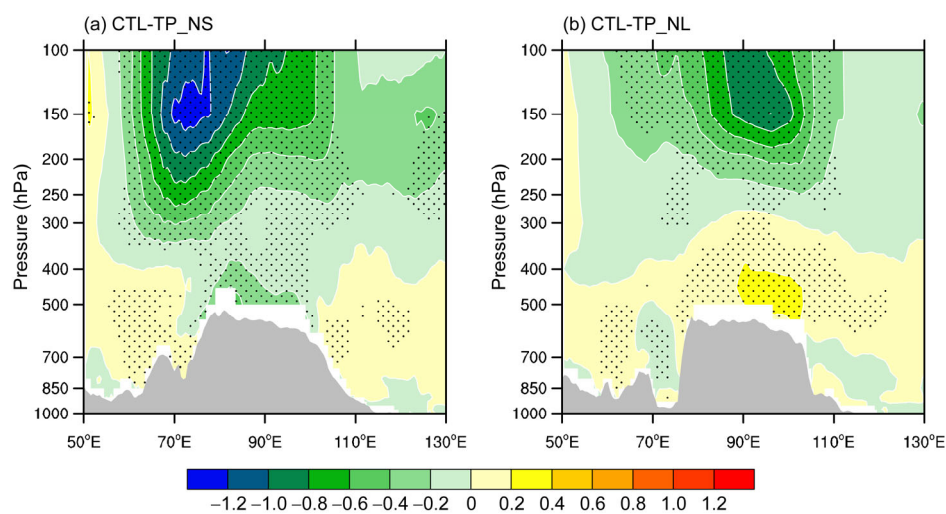


Figure 11 Potential vorticity difference exited by heating of the main body of the TP (unit: $\text{PVU} = 10^{-6} \text{ K m}^2 \text{ s}^{-1} \text{ kg}^{-1}$). (a) CTL minus TP_NS along 35°N due to surface sensible heating; (b) CTL-TP_NL along 32.5°N due to latent heating. Dotted regions denote statistical significance of the difference above the 95% level.

over South Asia, and shift its center northwestward; however, the impact of surface SH is stronger. The upper-layer anticyclonic circulation, induced by diabatic heating over the TP, is accompanied by warm temperatures at 300 hPa and by cold temperatures at 100 hPa, while its intensity at 100 hPa is stronger than at 300 hPa. The warm anticyclone in the upper troposphere is a deeper system, while the cold anticyclone aloft is a shallower system. Based on the thermal wind relation, it was shown that the anticyclone induced by TP heating is the strongest circulation near the tropopause, which favors the development of the AMC type of monsoonal meridional circulation.

By changing the configuration of temperature and circulation in the upper troposphere, diabatic heating of the TP can induce a prominent center of minimum potential vorticity near the tropopause. Because this center is located within the mid-latitude westerlies, it can excite a downstream-propagating Rossby wave train and thus, affect the circulation and climate of the Northern Hemisphere.

It is noted that two essential questions remain unsolved: how the warm anticyclone at 300 hPa is formed, and why this anticyclone changes to a cold system at 100 hPa. These issues will be discussed in the second part of this study.

Acknowledgements *The authors would like to thank the reviewers for their valuable comments and suggestions. This study was supported by the Nsionsl Natural Science Foundation of China (Grant Nos. 41275088, 91437219 & 41328006) and the the Special Fund for Public Welfare Industry (Meteorology) administered by the Chinese Ministry of Finance and the Ministry of Science and Technology (Grant No. GYHY201406001).*

References

- Bougeault P, Lacarrere P. 1989. Parameterization of orography-induced turbulence in a mesobeta-scale model. *Mon Wea Rev*, 117: 1872–1890
- Chang C P. 2004. *East Asian Monsoon*. Newssey: World Scientific. 564
- Chen F, Dudhia J. 2001. Coupling an advanced land-surface hydrology model with the Penn Statr-NCAR MM5 modeling system. Part I: Model implementation and sensitivity. *Mon Wea Rev*, 129: 569–585
- Chou M D, Suarez M J. 1999. A shortwave radiation parameterization for atmospheric studies. *NASA Tech Memo*, 15: 40
- Grell G, Devenyi D. 2002. A generalized approach to parameterizing convection combining ensemble and data assimilation techniques. *Geophys Res Lett*, 29: 31–38
- He B, Wu G X, Liu Y M, Bao Q. 2015. Astronomical and hydrological perspective of mountain impacts on the asian summer monsoon. *Sci Rep*, 5: 17586, doi: 10.1038/srep17586
- Held I M, Hou A Y. 1980. Nonlinear axially symmetric circulations in a nearly inviscid atmosphere. *J Atmos Sci*, 37: 515–533
- Hong S Y, Lim J. 2006. The WRF Single-Moment 6-Class microphysics scheme (WSM6). *J Korean Meteorol*, 42: 129–151
- Kim E J, Hong S Y. 2010. Impact of air-sea interaction on East Asian summer monsoon climate in WRF. *J Geophys Res*, 115: D19118
- Liu J, Wang Y, Wang A, Wang Y, Wang A, Hideaki O, Abbott R J. 2006. Radiation and diversification within the *Ligularia-Cremathodium-Parasenecio* complex (Asteraceae) triggered by uplift of the Qinghai-Tibetan Plateau. *Mol Phylogenet Evol*, 38: 31–49
- Luo H, Yanai M. 1984. The large-scale circulation and heat sources over the Tibetan Plateau and surrounding areas during the early summer of 1979. Part II: Heat and moisture budgets. *Mon Wea Rev*, 112: 966–989
- Mlawer E J, Taubman S J, Brown P D. 1997. Radiative transfer for inhomogeneous atmospheres: RRTM a validated correlated-k model for the long wave. *J Geophys Res*, 102: 16663–16682
- Plumb R A, Hou A Y. 1992. The response of a zonally symmetric atmosphere to subtropical thermal forcing: Threshold behavior. *J Atmos Sci*, 49: 1790–1799
- Reynolds R W, Smith T M, Liu C, Liu C, Chelton D B, Casey K S, Schlax M G. 2007. Daily high-resolution-blended analyses for sea surface temperature. *J Clim*, 20: 5473–5496
- Schneider E K, Lindzen R S. 1977. Axially symmetric steady-state models of the basic state for instability and climate studies. Part I: Linearized calculations. *J Atmos Sci*, 34: 263–279
- Schneider E K. 1977. Axially symmetric steady-state models of the basic state for instability and climate studies. Part II. Nonlinear calculations. *J Atmos Sci*, 34: 280–296
- Schneider E K. 1987. A simplified model of the modified Hadley circulation. *J Atmos Sci*, 44: 3311–3328
- Skamarock W C, Klemp J B, Dudhia J, Gill D O, Barker D M, Duda M G, Huang X Y, Wang W, Powers J G. 2008. A Description of the Advanced Research WRF Version 3. NCAR Technical Note NCAR/TN- 475+STR
- Smith E, Shi L. 1992. Surface forcing of the infrared cooling profile over the Tibetan plateau. Part I: Influence of relative longwave radiative heating at high altitude. *J Atmos Sci*, 49: 805–822
- Wang B. 2006. *The Asian Monsoon*. New York: Springer/Praxis Publishing. 787
- Wang Z Q, Duan A M, Wu G X. 2014. Impacts of boundary layer parameterization schemes and air-sea coupling on WRF simulation of the East Asian summer monsoon. *Sci China Earth Sci*, 57: 1480–1493
- Wang Z Q, Duan A M, Wu G X. 2014. Time-lagged impact of spring sensible heat over the Tibetan Plateau on the summer rainfall anomaly in East China: Case studies using the WRF model. *Clim Dyn*, 42: 2885–2898
- Wu G X, Liu Y M. 2000. Thermal adaptation, over flow, dispersion and subtropical anticyclone. I. Thermal adation and over flow (in Chinese). *Chin J Atmos Sci*, 24: 433–446
- Wu G X, Duan A M, Liu Y M, Mao J Y, Ren R C, Bao Q, He B, Liu B, Hu W T. 2015a. Recent progress in the study of Tibetan Plateau climate dynamics. *National Sci Rev*, 2: 100–116
- Wu G X, He B, Liu Y M, Bao Q, Ren R C. 2015b. Location and variation of the summertime upper troposphere temperature maximum over South Asia. *Clim Dyn*, 45: 1–18
- Wu G X, Li W P, Guo H, Liu H, Xue J X, Wang Z Z. 1997. The sensible heat driven air-pump of the Tibetan Plateau and the Asian summer monsoon. Collection for the Memory of Zhao Jiuzhang (in Chinese). Beijing: Science Press
- Wu G X, Liu Y M, He B, Bao Q, Duan A, Jin F. 2012. Thermal controls on the Asian Summer Monsoon. *Sci Rep*, 2: 404
- Wu G, Liu Y, Wang T, Liu X, Li W, Wang Z, Zhang Q, Duan, A, Liang X. 2007. The influence of the mechanical and thermal forcing of the Tibetan Plateau on the Asian climate. *J Hydrometeorol*, 8: 770–789
- Xu X, Lu C, Shi X, Ding Y. 2010. Large-scale topography of China: A factor for the seasonal progression of the Meiyu rainband. *J Geophys Res*, 115: D02110
- Xu X, Lu C, Shi X, Gao S. 2008a. World water tower: An atmospheric perspective. *Geophys Res Lett*, 35: L20815
- Xu X, Shi X, Wang Y, Shi X. 2008b. Data analysis and numerical simulation of moisture source and transport associated with summer precipitation in the Yangtze River Valley over China. *Meteorol Atmos Phys*, 100: 217–231
- Yanai M, Li C, Song Z. 1992. Seasonal heating of the Tibetan Plateau and its effects on the evolution of the Asian summer monsoon. *J Meteor Soc Japan*, 70: 319–351
- Yanai M, Wu G. 2006. Effects of the Tibetan Plateau. *Asian Monsoon*, 29: 513–549
- Yang H W, Wang B, Wang B. 2012. Reduction of systematic biases in regional climate downscaling through ensemble forcing. *Clim Dyn*, 25: 155–170
- Ye D Z and Gao Y X. 1979. *Tibetan Plateau Meteorology* (in Chinese). Beijing: Science Press
- Zhao P, Chen L X. 2001. Interannual variability of atmospheric heat source/sink over the Qinghai-Xizang (Tibetan) Plateau and its relation to circulation. *Adv Atmos Sci*, 18: 106–116
- Zhou X J, Zhao P, Chen J M, Chen L X, Li W P. 2009. The impact of the thermal forcing of the Tibetan Plateau on the climate of the northern hemisphere. *Sci China Ser D-Earth Sci*, 52: 1679–1693